Electronic Supplementary Material (ESI) for Nanoscale.
This journal is © The Royal Society of Chemistry 2020

Electronic Supplementary Information

Observation of Coupled Mechanical Resonance Modes within Suspended 3D Nanowire Arrays

1. 3D Nanowire Array Fabrication

3D NW arrays in the form of vertical NW stacks are fabricated on a 4”-diameter, <100> silicon-on-insulator (SOI) wafer with the device, buried oxide (BOX) and handle layer thicknesses of 1±0.1 µm, 1 µm and 725 µm, respectively. The 1-µm-thick SOI device layer is particularly selected, as it facilitates the fabrication of a large number of NWs. Although similar stacks were previously reported for a variety of purposes including gate-all-around field-effect-transistors [1] and MEMS manipulators [2], the introduction of common couplers and side-gate electrodes allows the study of collective dynamic characteristics exhibited by such vertical NW arrays.

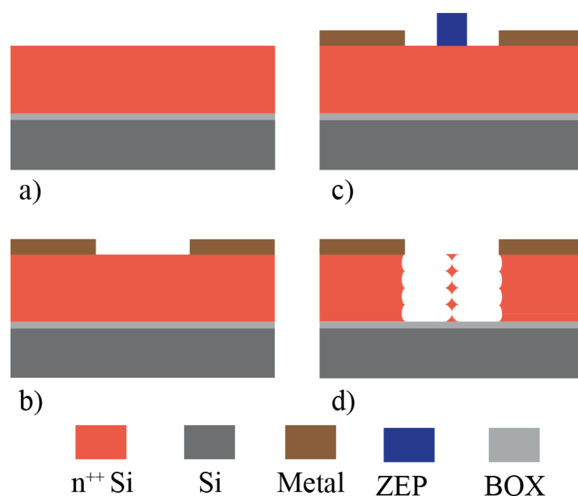

Figure S1: Fabrication process developed to fabricate 3D NW arrays in the form of vertical stacks along with couplers and side-gate electrodes. a) device layer doping and wafer dicing, b) metallization by lift-off, c) e-beam patterning of Si NW and coupler, d) Si deep etch through Bosch process.

The fabrication flow is summarized briefly in Fig. S1. After the initial cleaning of the SOI wafer by RCA (RCA1+RCA2) and HF, the device layer of the SOI wafer is doped with phosphorus to approximately 10^{20} cm^{-3} at the wafer surface. Next, the wafer is annealed at 900 °C for 30 minutes to enhance doping uniformity across the device layer thickness. This doping level is adopted to obtain ohmic contact between Si and the subsequent metal layer [3] and to reduce the temperature dependence of the piezoresistive coefficient of Si [4]. First, e-beam lithography (Vistec EBPG5000) is carried out with the PMMA (poly methyl methacryllate) bilayer resist to deposit metal (5 nm Cr and 50 nm Pt) alignment marks through a lift-off process. Metal films are deposited through e-beam evaporation (Leybold Optics LAB 600H). Then the wafer is diced into 1 cm x 1 cm chips by Disco DAD321 automatic dicing saw (Fig. S1.a). Dicing is carried out for the subsequent chip-level deep reactive ion etching (DRIE) optimization as such dice are used to perform etching characterization. Next, the first e-beam lithography process is repeated with the same PMMA bilayer resist structure to deposit metal touchpads, lines and electrodes on each die (Fig. S1.b). A third e-beam lithography is carried out to define the NW and coupler mask with the ZEP520A 100% e-beam resist by Zeon Corp (Fig. S1.c). Bosch process is employed (Alcatel AMS200 SE) to fabricate a vertical NEMS stack which is

electrically isolated from adjacent electrodes (Fig. S1.d). Since this is the most critical step for obtaining vertical NW stacks, an optimization study is performed as detailed below. Exposed region of the SOI device layer is etched until the underlying BOX layer to form electrodes and couplers. Finally, the resist is removed in oxygen plasma (Tepla Gigabatch) (Fig. S1.d). In this way, a vertical SiNW stack with common couplers is fabricated with the couplers remaining attached to the underlying BOX layer.

Bosch process is essentially a fluorine-based deep etch process that consists of alternating steps of isotropic plasma etching in SF_6 and passivation with C_4F_8. Tuning of this etch step is critical as it sets the extent of the undercut. Hence, either an array of released Si NWs or a fin can form depending on the extent of etch scallops [5-7]. Both the etch rate of the Bosch process and the resulting NW profile are governed by loading, microloading and ion-induced defluorination of the passivation film [5]. Sample layout parameters, chamber base pressure, plasma power, gas flow rates and duration of each etch step constitute main parameters of the process. Layout parameters determine local etch rate and ultimately NW profile through microloading and aspect ratio dependent etching (ARDE). Die-level process optimization requires employment of a 4'' dummy blank base wafer to control the loading effect. On the other hand, microloading effect manifests itself as local etch rate degradation due to replenishment difficulty of etchant species inside a trench [8].

In this context, etch step time and layout parameters are investigated to reach an optimum vertical NW stack structure. Otherwise, strong sensitivity of NW profile on deep etch parameters results in faulty structures such as completely etched or partially released NWs. In this respect, insertion of a purge step between small groups of etch cycles is found to improve stack uniformity. As a result of a systematic deep etch characterization, the etch recipe optimized in terms of NW uniformity and structural integrity is shown in Table S1. This recipe is used to realize vertical stacks consisting of 7 Si NWs. Moreover, couplers in the form of membranes with lengths ranging from 5% (100 nm) to 50% (1000 nm) of the length of adjoined 2-µm-long NWs are fabricated.

Table S1: Bosch process parameters optimized to enhance NW uniformity in a vertical stack.

SF_6 flow rate (cm^3/min)	**SF6 etch duration (s)**	**C_4F_8 flow rate (cm^3/min)**	**C_4F_8 etch duration (s)**	**Power (W)**	**Base Pressure (mbar)**
300	2.3	150	1	600	10^{-7}

Fig. 2.a of the manuscript shows that complete etching of the SOI device layer results in vertical stacks of 7 free-standing NWs. The number of NWs within a vertical stack is adjusted conveniently by setting the number of etch cycles. In accordance with the literature [9], (n) number of etch cycles results in (n-1) NWs. Thus, number of NWs is set by the device layer thickness and the scallop size. Accordingly, etching of a layer of thickness h with (n) NWs requires a scallop size of approximately $h/2n$. Hence, the recipe in Table S1 provides a scallop size of approximately 60 nm.

For proper isolation of the electrodes from the NW-coupler blocks, complete elimination of Si in between is very critical. Considering the trench aspect ratios involved and the dielectric nature of the BOX layer serving as an etch stop, this becomes a challenging task. As a solution, extra etching cycles have to be employed for complete removal of any remaining Si film. Thus, 11 etch cycles - corresponding to a process time of 37 s with the etch recipe of Table S1 - are used. Microscopic examination of fabricated NW arrays reveals a certain reduction in NW

width from the nominal mask linewidth of 100 nm to 60 nm. In addition, selection of larger coupler widths relative to NWs ensures fabrication of solid couplers as shown in Fig. 2.a.

2. Coupled NW Array Modeling

Although the idea of mechanical coupling and the associated introduction of collective modes are interesting, the addition of a coupling element into the overall picture necessitates its proper design for a successful device implementation [10]. Electromechanical modeling of a single MEMS/NEMS resonator is based on well-established analytical techniques [10-12]. However, these techniques cannot be borrowed to model coupling membranes directly. In the literature, an analytical approach known as quarter-wavelength ($\lambda/4$) modeling is employed to design coupling beams [13, 14]. However, analytical solutions are only available for a limited number of couplers having specific boundary conditions. Contrary to conventional coupling beams [15], one side surface of each common coupling membrane of this work is fixed. Hence, this boundary condition modification requires new coupling modeling methodology.

Let us consider a resonator array which consists of 7 harmonic resonators. In Fig. S2, each resonator is represented with equivalent mass (m_r), damping (c_r) and stiffness (k_r) parameters determined analytically [10]. In this lumped-parameter modeling, each coupling between sequential resonators is modeled with spring and mass elements. The coupling between non-adjacent resonators is neglected to simplify the mechanical model, which proved to be adequate to capture basic physics.

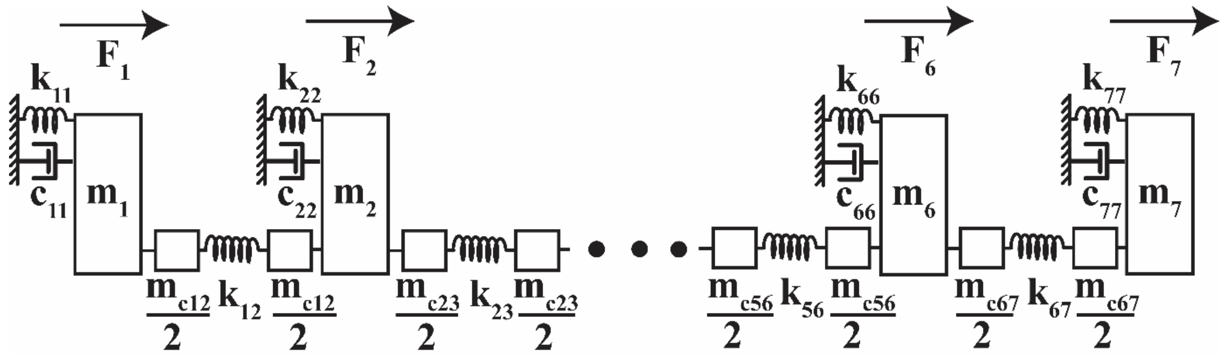

Figure S2: In order to simplify modeling of a coupled NW array, couplers consisting of mass and spring elements are considered between sequential NWs.

Equation of the motion of the mechanical model of Fig. S2 is derived in the following generalized compact form:

$$\boldsymbol{M}\ddot{\boldsymbol{x}} + \boldsymbol{C}\dot{\boldsymbol{x}} + \boldsymbol{K}\boldsymbol{x} = \boldsymbol{f}\cos(\omega t) \tag{1}$$

in which $\boldsymbol{M}$, $\boldsymbol{C}$, $\boldsymbol{K}$ are n×n mass, damping and stiffness matrices, respectively, for a system with n degrees of freedom, whereas $\boldsymbol{f}$, $\boldsymbol{x}$, $\dot{\boldsymbol{x}}$ and $\dot{\boldsymbol{x}}$ represent force, displacement, velocity and acceleration vectors, respectively. Reduction of these second-order differential equations to first-order equivalents by defining $v_i = dx_i/dt$ as new variables leads to a matrix equation of the form:

$$\boldsymbol{A}\dot{\boldsymbol{y}} + \boldsymbol{B}\boldsymbol{y} = \boldsymbol{f}\cos(\omega t) = \boldsymbol{f}\left\{e^{i\omega t} + e^{-i\omega t}\right\}/2 \tag{2}$$

where $\boldsymbol{y}$ is a 1×2n vector containing unknown velocities and positions of the masses. Assumption of a solution in the form of $\boldsymbol{y} = \boldsymbol{Y_o}e^{i\omega t}$ results in the following relation by substituting into Eq. 2:

$$(i\omega\boldsymbol{A} + \boldsymbol{B})\boldsymbol{Y_o} = \boldsymbol{f} \tag{3}$$

Thus, the steady-state response of the mechanical model of Fig. S2 is found as:

$$\boldsymbol{y}(t) = \left(\boldsymbol{Y_o}e^{i\omega t} + \overline{\boldsymbol{Y_o}}e^{-i\omega t}\right)/2 \tag{4}$$

The vibration of jth mass has the following form:

$$x_j(t) = X_j \cos(\omega t + \varphi_j) \tag{5}$$

where $X_j = \sqrt{Y_j \overline{Y_j}}$ and $\varphi_j = \log(\overline{Y_j}/Y_j)/2i$ are the amplitude and phase of the harmonic response of each mass, respectively. Thus, the coupled second-order equations of Eq. 1 can be solved numerically following this procedure. Summation of the spectrum response of each resonator results in the overall response of the coupled resonator array.

The equivalent mass, spring and damping parameters of each NW in Fig. S2 are determined with the knowledge of its dimensions and material properties. However, cross-sectional variation for each NW and between NWs due to local etch rate alteration coupled with the small gap between a NW stack and its electrodes complicate NW dimensional characterization. Thus, finite element modeling (FEM) is employed to match the modes of a NW stack to the measured modal frequencies first. In this way, mean cross-sectional dimensions of each NW are found by considering gradual increase of dimensions towards the lowermost NW. On the other hand, since the coupling element is fixed to the substrate, the gradual increase of coupling element stiffness from the highest to lowest NW is taken into account in the numerical model. However, the same coupling mass value is used for each coupling element in Fig. S2. Moreover, the presence of the thin metal film on the top electrode surface — along with the inevitable doping profile heterogeneity lead to an increased transduction efficiency and hence preferable excitation of the top NW within each stack. Thus, the gradual decrease of electrostatic force towards the undermost NW is predicted. Furthermore, the damping element of each NW is calculated with the Q of 500 in accordance with measured Q values of the array modes. Within this scope, the lumped model parameters in Fig. S2 are determined to analyze the detected modes of coupled NW arrays.

FEM of the coupled vertical NW arrays is performed with a commercial analysis software with 3D free-tetrahedral mesh elements. More than 35000 mesh elements are utilized to carry out modal analyses. In this way, FEM is used to analyze the effect of various parameters including boundary conditions of the coupler and the variations in NW dimensions on modal frequencies and mode shapes. Fig. S3 provides one such comparative study for the mode shape of the first flexural mode of Fig. 1b of the manuscript. Here, seven modal frequencies are closely spaced within the narrow band of 92.0 MHz – 93.3 MHz. First, the couplers are considered attached to the bottom surface, *i.e.* the BOX layer of the substrate, while NW dimensions are kept uniform throughout the stack. This leads to some degree of suppression of the deflection of the lowest NWs with no significant change of modal frequencies (upper right). If up to 13% variation of the NW width is allowed, a different picture emerges (lower left). The frequency band becomes wider covering the range between 92.7 MHz to 104.8 MHz. In addition, mode shapes also change. The uppermost NWs seem to interact to a higher degree in lower modes, while lower NWs contribute to higher modes on an individual basis with limited interaction among each other. Fixing the coupler bottom in this case further limits these interactions (lower right). Out-of-plane modes in all instances appear above 130 MHz, thereby eliminating the possibility of having encountered them in the measurements of Figs. 1 and 2 of the manuscript.

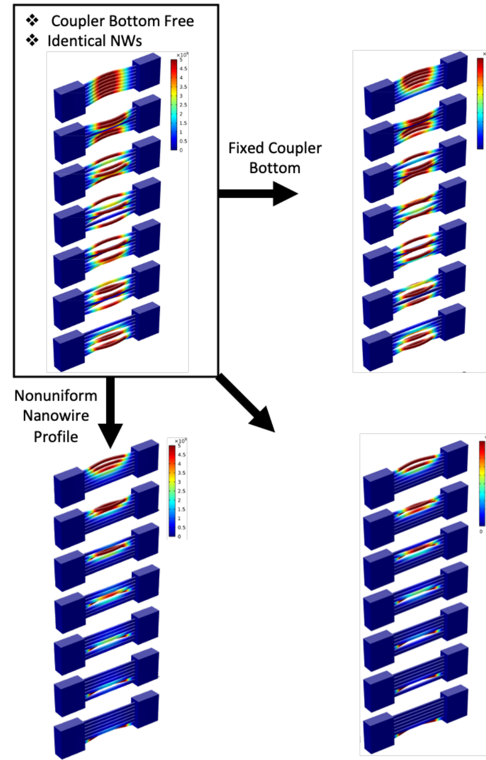

Figure S3: The effect of coupler boundary conditions and NW dimensional uniformity within the array on mode shapes. The upper left case corresponds to that of Fig. 1b.

3. Frequency Spectrum Measurements

Spectral measurements are carried out by two different frequency downmixing schemes: 1ω and 2ω. Experimental setups shown schematically in Fig. S4.a-b for each downmixing technique are similar to those reported elsewhere [16, 17]. The 1ω downmixing scheme results in output signals at the driving frequency (ω) whose magnitude is proportional to vibration amplitude and static deflection at rest. On the contrary, output signals from the 2ω method are at the frequency of 2ω and depend only on the square of vibration amplitude. Tensile stress stemming from undercut of supports was attributed to higher static deflections for top-down devices in the literature [16]. Hence, more efficient motion transduction to electrical signals is expected with the 1ω technique in our case of NW stacks fabricated using the aforementioned top-down approach. Comparison of readout signals through both the 1ω and 2ω schemes at a common set of measurement parameters for one device (Sample 4) is given in Fig. S4.c. Fig. S4.c indicates that the 2ω method leads to signal amplitudes considerably lower than those of 1ω in general. Thus, spectrum measurements are performed with the 1ω scheme.

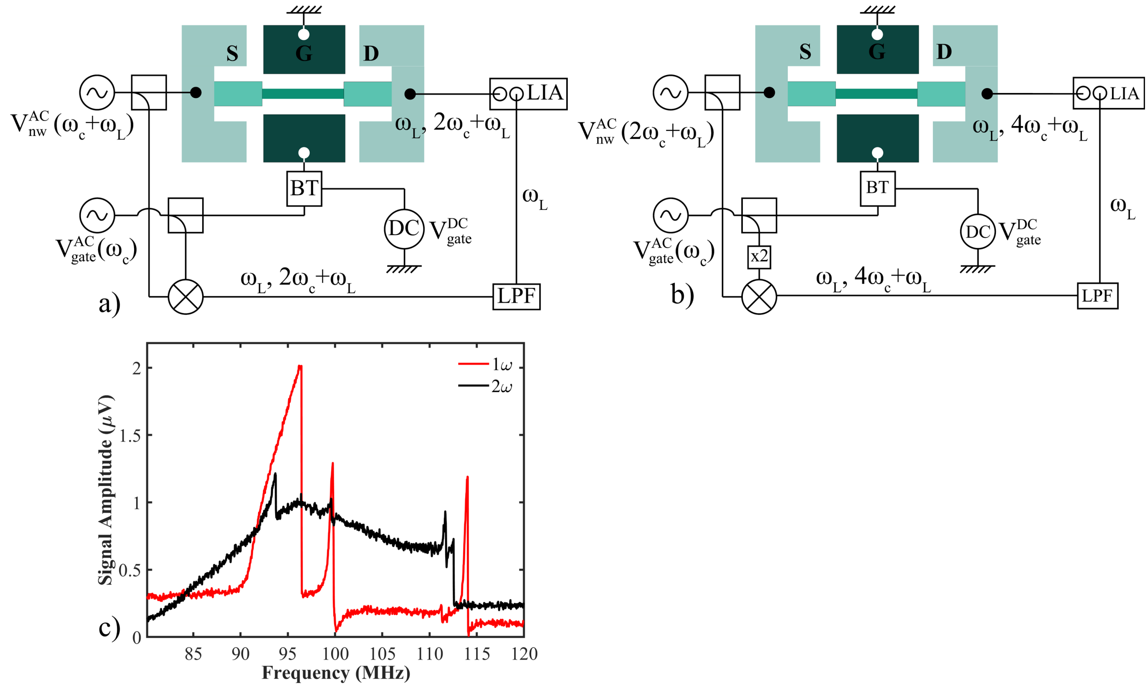

Figure S4: Schematics of the a) 1ω and b) 2ω downmixing schemes. LIA: Lock-in Amplifier, LPF: Low Pass Filter, BT: Bias Tee c) Although providing resolvable resonance peaks in this case, the 2ω method leads to significantly lower signal amplitudes in general. $V_{gate}^{DC} = 15\ V$, $V_{gate}^{AC} = 0.36\ V_{pp}$ and $V_{NW}^{AC} = 0.25\ V_{pp}$

4. Mode Splitting and Mode Coupling

NW array modes existing in close proximity exhibit a spectrum behavior similar to the typical spectrum response of a bandpass filter. Evolution of spectrum characteristics of such modes is tracked with respect to gate DC and AC voltages in Fig. S5.a-b. Moreover, coupled vertical NEMS stacks with various architectures also result in similar spectrum characteristics. For example, Fig. S5.c shows such adjacent modes for a coupled vertical NEMS stack with a coupling length of 500 nm.

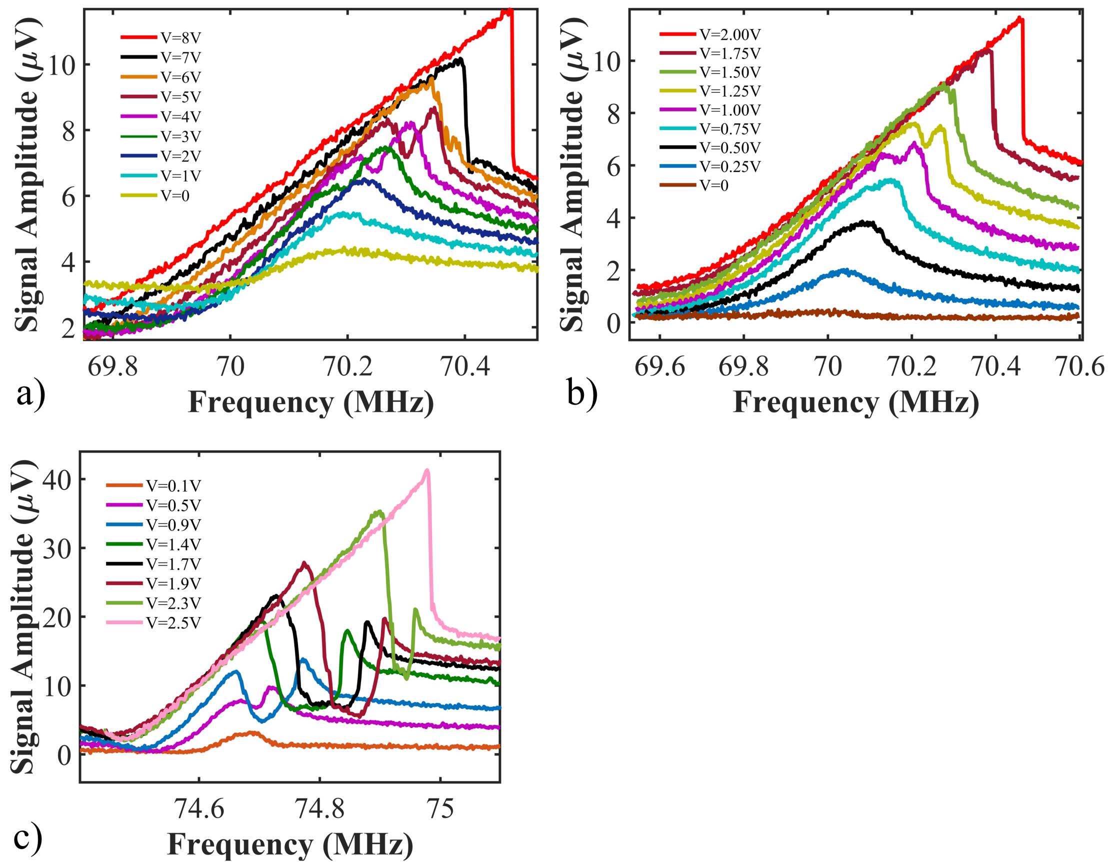

Figure S5: Evolution of spectrum characteristics of modes in close proximity with respect to a) gate DC and b) gate AC voltages. c) Adjacent modes of a coupled vertical NEMS stack with a coupling length of 500 nm are tracked with respect to gate AC voltages.

Signal response comparison of nominally identical NW stacks coupled either with stiff (L_c =100 nm) or compliant couplers (L_c =1000 nm) is performed to demonstrate the dependence of Q on coupler stiffness. Fig. S6 illustrates that Q of a coupled mode decreases by switching to more compliant coupling as expected. Hence, there is a trade-off between more interaction of NWs in a stack and additional damping in couplers by increasing coupler compliance.

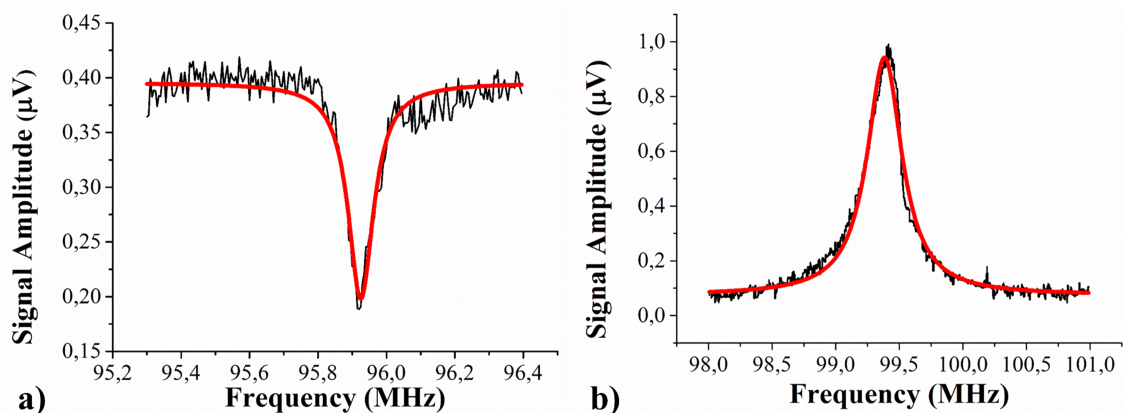

Figure S6: Lorentzian fits to the modes of NW stacks incorporating either a) stiff or b) compliant couplers reveal Qs of 1062 and 298 respectively.

Mode coupling measurements are performed using a setup similar to the 1ω downmixing scheme shown in Fig. S4.a. In this case, NW and gate voltage signals now have two

components, one for each mode as shown in Fig. S7. Voltages employed in the mode coupling measurements in Fig. 4 for each coupling case are provided in Table S2.

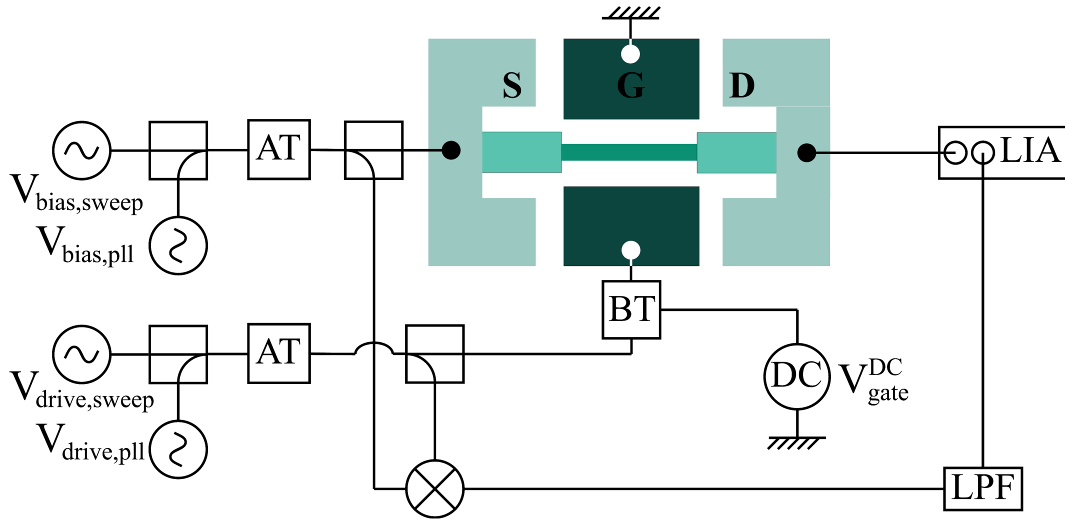

Figure S7: Schematics of the setup used to perform mode coupling measurements. Unlike the previous schemes, NW and gate AC voltage signals now have two components, one for each mode. LIA: Lock-in Amplifier, LPF: Low Pass Filter, BT: Bias Tee, AT: Attenuator

Table S2. Drive voltages employed in mode coupling measurements in Fig. 4 for each coupling case prevent direct comparison of resulting frequency shifts to determine coupling strengths.

<table>
<tr><th>Voltages</th><th>Stiff Coupling</th><th>Compliant Coupling</th></tr>
<tr><td>$V_{bias, sweep}$ (V_{pp})</td><td colspan="2">0.6</td></tr>
<tr><td>$V_{bias, pll}$ (V_{pp})</td><td colspan="2">0.8</td></tr>
<tr><td>$V_{drive, sweep}$ (V_{pp})</td><td>0.8</td><td>2</td></tr>
<tr><td>$V_{drive, pll}$ (V_{pp})</td><td>4</td><td>0.8</td></tr>
<tr><td>$V_{gate, DC}$ (V)</td><td>15.4</td><td>9</td></tr>
</table>

References

[1] M. D. Marchi *et al.*, "Top–Down Fabrication of Gate-All-Around Vertically Stacked Silicon Nanowire FETs With Controllable Polarity," *IEEE Transactions on Nanotechnology,* vol. 13, no. 6, pp. 1029-1038, 2014.

[2] O. Ozsun *et al.*, "Monolithic Integration of Silicon Nanowires With a Microgripper," *Journal of Microelectromechanical Systems,* vol. 18, no. 6, pp. 1335-1344, 2009.

[3] P. E. Allain, F. Parrain, A. Bosseboeuf, S. Mâaroufi, P. Coste, and A. Walther, "Large-Range MEMS Motion Detection With Subangström Noise Level Using an Integrated Piezoresistive Silicon Nanowire," *Journal of Microelectromechanical Systems,* vol. 22, no. 3, pp. 716-722, 2013.

[4] A. A. Barlian, W.-T. Park, J. R. Mallon, Jr., A. J. Rastegar, and B. L. Pruitt, "Review: Semiconductor Piezoresistance for Microsystems," (in eng), *Proceedings of the IEEE. Institute of Electrical and Electronics Engineers,* vol. 97, no. 3, pp. 513-552, 2009.

[5] M. Zervas, D. Sacchetto, G. De Micheli, and Y. Leblebici, "Top-down fabrication of very-high density vertically stacked silicon nanowire arrays with low temperature budget," *Microelectronic Engineering,* vol. 88, no. 10, pp. 3127-3132, 2011.

[6] D. Sacchetto, M. H. Ben-Jamaa, G. DeMicheli, and Y. u. Leblebici, "Fabrication and characterization of vertically stacked Gate-All-Around Si Nanowire FET arrays," in *2009 Proceedings of the European Solid State Device Research Conference*, 2009, pp. 245-248.

[7] D. Sacchetto *et al.*, "Vertically-stacked gate-all-around polysilicon nanowire FETs with sub-μm gates patterned by nanostencil lithography," *Microelectronic Engineering,* vol. 98, pp. 355-358, 2012.

[8] C. Hedlund, H. O. Blom, and S. Berg, "Microloading effect in reactive ion etching," vol. 12, no. 4, pp. 1962-1965, 1994.

[9] R. M. Y. Ng, T. Wang, and M. Chan, "A New Approach to Fabricate Vertically Stacked Single-Crystalline Silicon Nanowires," in *2007 IEEE Conference on Electron Devices and Solid-State Circuits*, 2007, pp. 133-136.

[10] F. D. Bannon, J. R. Clark, and C. T. C. Nguyen, "High-Q HF microelectromechanical filters," *IEEE Journal of Solid-State Circuits,* vol. 35, no. 4, pp. 512-526, 2000.

[11] Y. Xie, S. S. Li, Y. W. Lin, Z. Ren, and C. T. C. Nguyen, "1.52-GHz micromechanical extensional wine-glass mode ring resonators," *IEEE Transactions on Ultrasonics, Ferroelectrics, and Frequency Control,* vol. 55, no. 4, pp. 890-907, 2008.

[12] M. Akgul, L. Wu, Z. Ren, and C. T. C. Nguyen, "A negative-capacitance equivalent circuit model for parallel-plate capacitive-gap-transduced micromechanical resonators," *IEEE Transactions on Ultrasonics, Ferroelectrics, and Frequency Control,* vol. 61, no. 5, pp. 849-869, 2014.

[13] W. Kun and C. T. C. Nguyen, "High-order medium frequency micromechanical electronic filters," *Journal of Microelectromechanical Systems,* vol. 8, no. 4, pp. 534-556, 1999.

[14] M. U. Demirci and C. T. C. Nguyen, "Higher-mode free-free beam micromechanical resonators," in *IEEE International Frequency Control Symposium and PDA Exhibition Jointly with the 17th European Frequency and Time Forum, 2003. Proceedings of the 2003*, 2003, pp. 810-818.

[15] C. T. c. Nguyen, "MEMS technology for timing and frequency control," *IEEE Transactions on Ultrasonics, Ferroelectrics, and Frequency Control,* vol. 54, no. 2, pp. 251-270, 2007.

[16] M. Sansa, M. Fernández-Regúlez, J. Llobet, Á. San Paulo, and F. Pérez-Murano, "High-sensitivity linear piezoresistive transduction for nanomechanical beam resonators," *Nature Communications,* vol. 5, no. 1, p. 4313, 2014.

[17] M. Nasr Esfahani *et al.*, "Piezoresistive silicon nanowire resonators as embedded building blocks in thick SOI," *Journal of Micromechanics and Microengineering,* vol. 28, no. 4, p. 045006, 2018.